Visible-Light-Driven Cuprous Oxide Nanomotors with Surface Heterojunction-Induced Propulsion

Wenjuan Liu,*[ab] Xiao Chen,[a] Xiaoyong Ding,[a] Qiang Long,[a] Xiaolong Lu,*[c] Qiang Wang [d]* and Zhongwei Gu[ab]

a College of Materials Science and Engineering, Nanjing Tech University, Nanjing 211816, China

b Jiangsu Collaborative Innovation Center for Advanced Inorganic Functional Composites, Nanjing Tech University, Nanjing 211816, China

c State Key Laboratory of Mechanics and Control of Mechanical Structures, Nanjing University of Aeronautics and Astronautics, Nanjing 210016, China

d School of Chemistry and Molecular Engineering Nanjing Tech University, Nanjing 211810, China

Corresponding authors:

Wenjuan Liu: liuwenjuan@njtech.edu.cn

Xiaolong Lu: long_8446110@nuaa.edu.cn

Qiang Wang: wangqiang@njtech.edu.cn

Video S1: Movement of truncated octahedral and spherical Cu_2O micro/nanomotors in ultra-pure water and 0.01% H_2O_2 solution under ambient light.

Video S2: Cu_2O nanomotors in ultra-pure water under different light sources.

Video S3: Cu_2O nanomotors in 0.01% H_2O_2 under different light sources.

Video S4: Negative phototactic behavior of Cu_2O nanomotors in different solutions under blue point light source.

Possible photocatalytic mechanism

Owning to the limited penetration depth of light in semiconductor, asymmetric concentration gradients of photocatalytic products will be generated on the surface of the photocatalyst under visible light irradiation, producing the autonomous motion of corresponding motors in the form of diffusiophoresis.[1,2] Analogously, Cu_2O crystals can create holes (h^+) and electrons (e^-) within the visible region of the spectrum. Moreover, it is well recognized that Cu_2O has a strong adsorption capacity for oxygen molecules (O_2).[3] The photogenerated electrons migrated to the crystal surface can react with the adsorbed O_2 to produce superoxide anion free radicals ($\cdot O_2^-$). The $\cdot O_2^-$ reaction with H_2O can further result in the formation of hydroxyl ions (OH^-) and hydroxyl radicals ($\cdot OH$). Meanwhile, the photogenerated holes accumulated on the facets of the Cu_2O crystals can react with OH^- to generate $\cdot OH$. The possible catalytic cycle is given below:

$$Cu_2O + hv \rightarrow e^- + h^+ \tag{2}$$

$$O_2 + e^- \rightarrow \cdot O_2^- \tag{3}$$

$$2H_2O + \cdot O_2^- + 2e^- \rightarrow 3OH^- + \cdot OH \tag{4}$$

$$OH^- + h^+ \rightarrow \cdot OH \tag{5}$$

Thus, ideally, without any additional surface modification, single-component Cu_2O micro/nanomotors could present good optical response in the visible light range. However, photocorrosion effect leads to a poor photogenerated charges separation/transport capability of Cu_2O, thereby reducing its photocatalytic activity. As mentioned above, apart from forming heterojunction with other materials, engineering crystal facet is also helpful to improve Cu_2O performance.

References

[1] J. Wang, Z. Xiong, J. Zheng, X. Zhan and J. Tan, *Acc. Chem. Res.*, 2018, **51**, 1957-1965.

[2] W. Wang, W. Duan, S. Ahmed, T. E. Mallouk, A. Sen, *Nano Today*, 2013, **8**, 531-554.

[3] L. Tang, J. Lv, S. Sun, X. Zhang, C. Kong, X. Song, Z. Yang, *New J. Chem.*, 2014, **38**, 4656-4660.

Fig. S1 Schematic diagram of preparation process and optical photo of Cu_2O particulates.

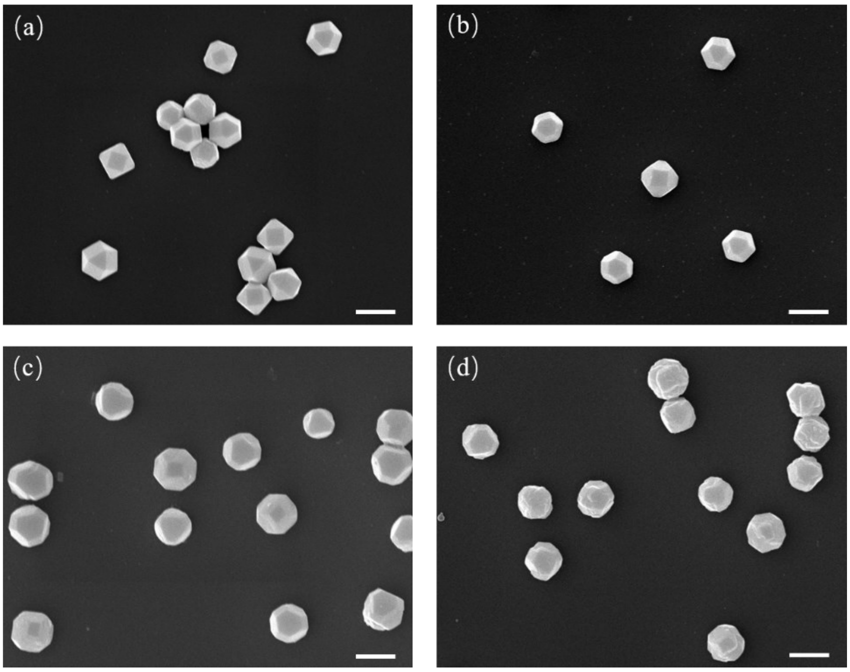

Fig. S2 SEM of Cu_2O micro/nanomotor synthesized by different dosage of PVP 0.5 g (a), 1.0 g (b), 1.8 g (c), 3.5 g (d), respectively. Scale bar: 1μm.

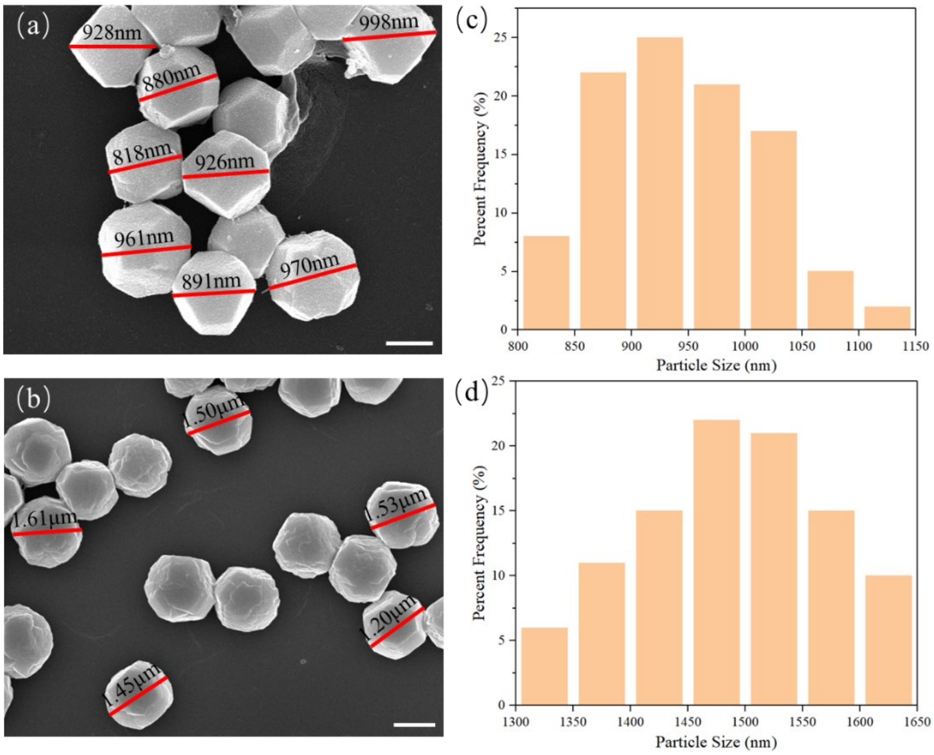

Fig. S3 Size distribution histograms for truncated octahedral Cu_2O nanomotors (a) and spheroidal Cu_2O micromotors (b).

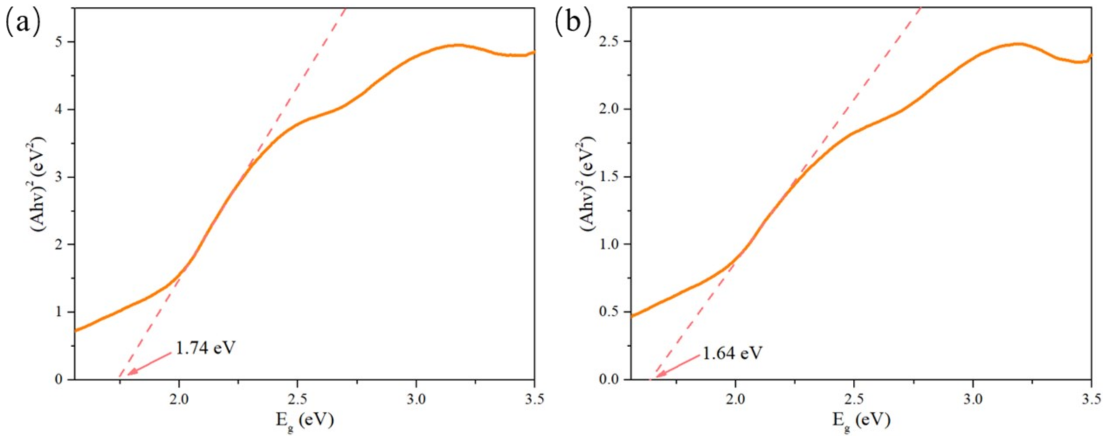

Fig. S4 Band gap energy of Cu_2O micro/nanomotors with spherical (a) and truncated octahedral structure (b), respectively.

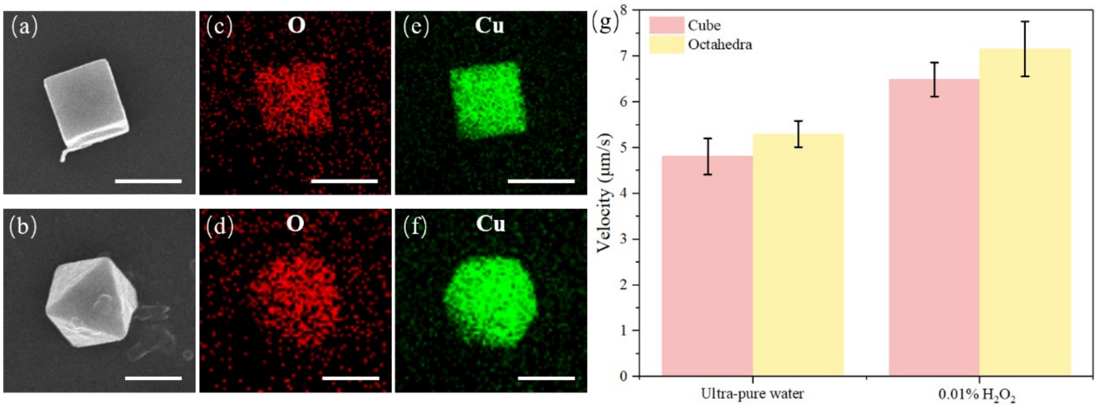

Fig. S5 SEM images of Cu_2O micro/nanomotors with cubic (a) and octahedral structures (b). EDX mapping images for O and Cu elemental distribution of cubic (c)&(e) and octahedral (d)&(f) Cu_2O micro/nanomotors, respectively. (e) Velocity of cubic and octahedral Cu_2O motors in ultra-pure water and 0.01 v% H_2O_2 solution under ambient light exposure.

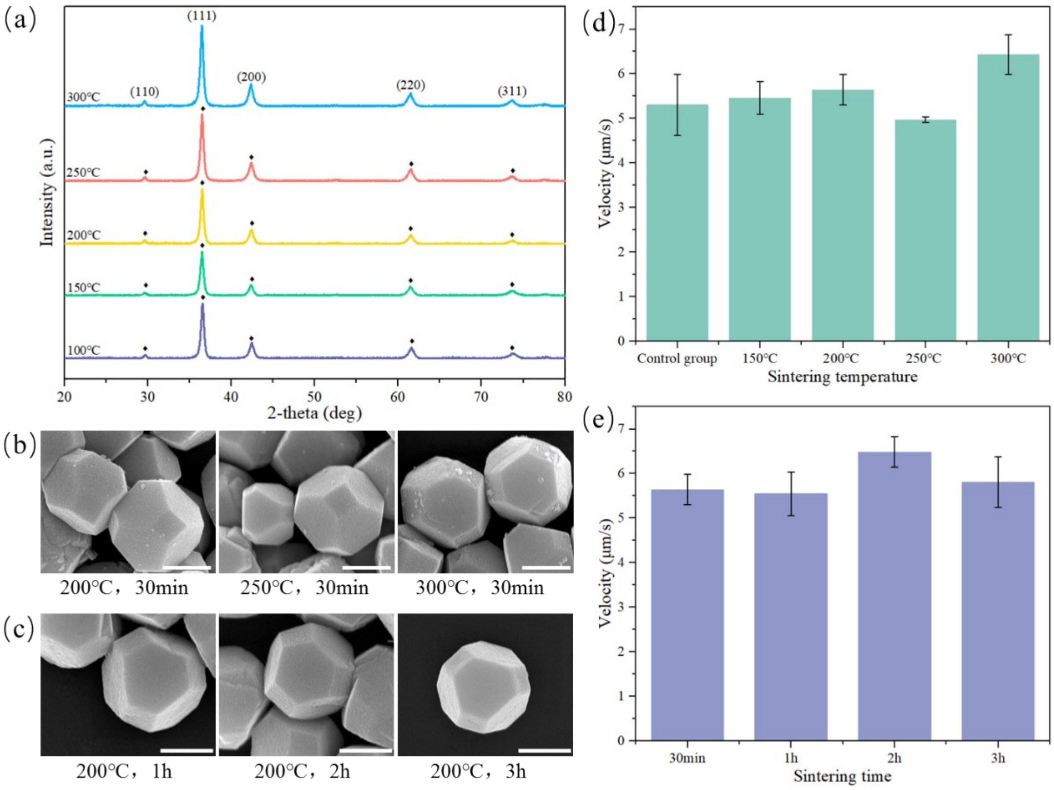

Fig. S6 Influence of heat treatment on the structure and motion speed of truncated octahedral Cu_2O nanomotors. XRD patterns of Cu_2O nanomotors after heat treatment at different sintering temperature for 30 min (a); SEM images of Cu_2O nanomotors after different heat treatment process: different sintering temperature for 30 min (b), different sintering time at 200 ℃ (c); Speed of Cu_2O nanomotors under ambient light in pure water after different heat treatment process: different sintering temperature for 30 min (d), different sintering time at 200 ℃ (e). Scale bar: 500 nm.

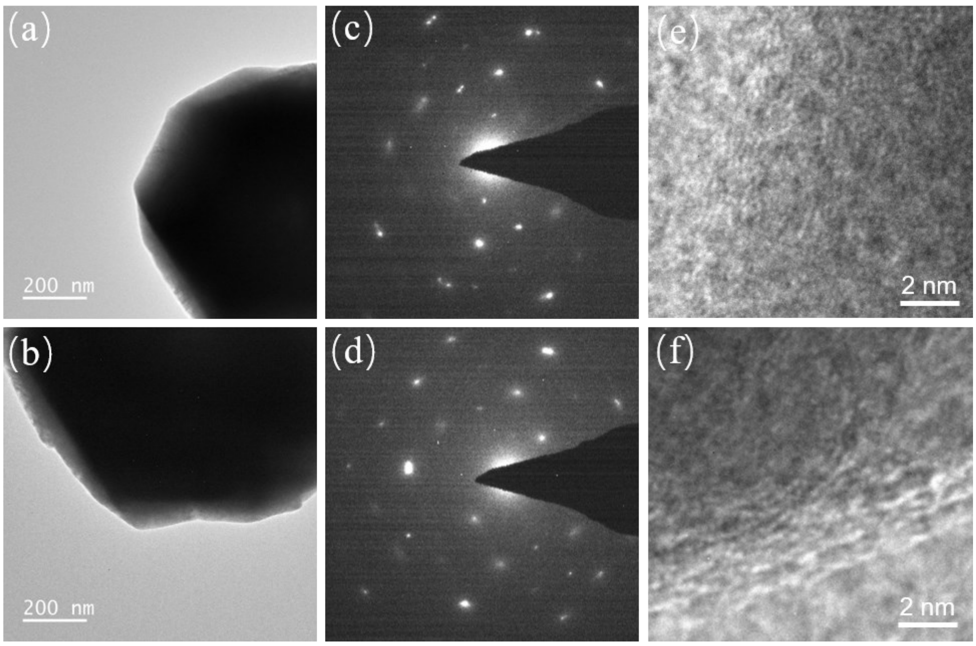

Fig. S7 Detailed morphology and crystal structure for spherical Cu_2O micromotors. TEM images (a, b), SAED patterns (c, d), and high-resolution TEM images (e, f).

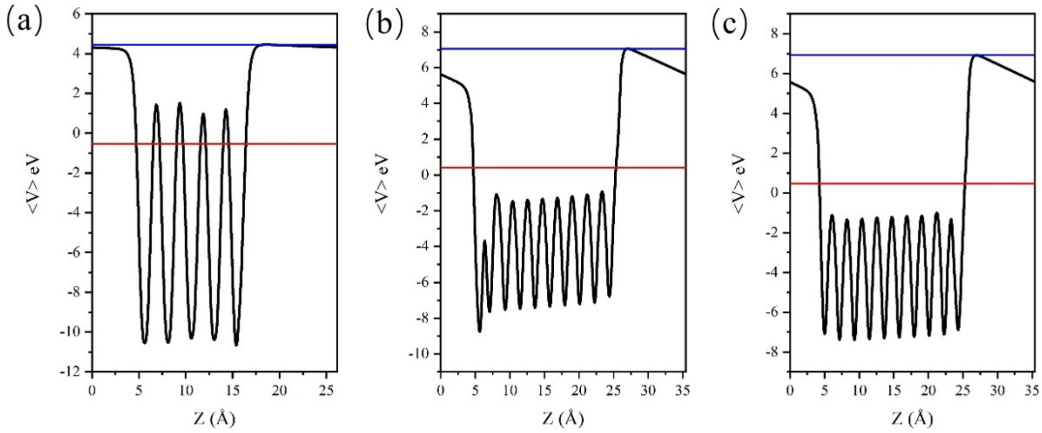

Fig. S8 Work function of Cu_2O(111) (a), (100)Cu (b) and (100)O (c) surfaces.

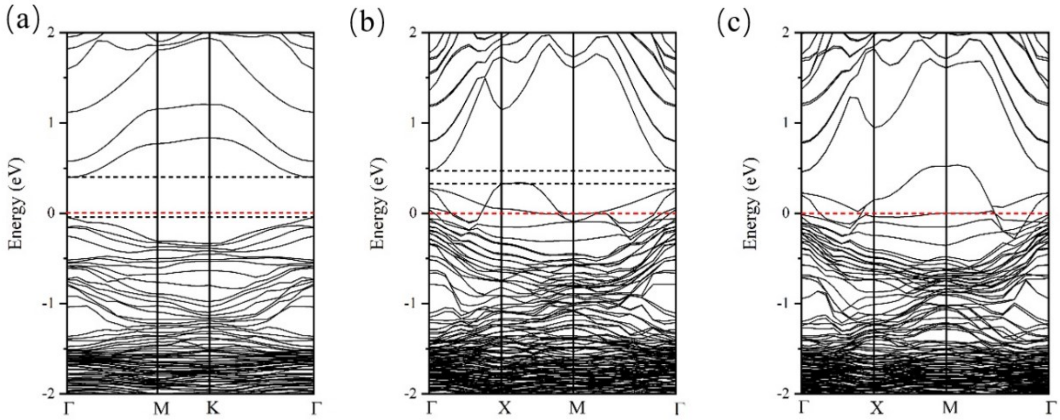

Fig. S9 Energy band structures of Cu_2O(111) (a), (100)Cu (b) and (100)O (c) surfaces.

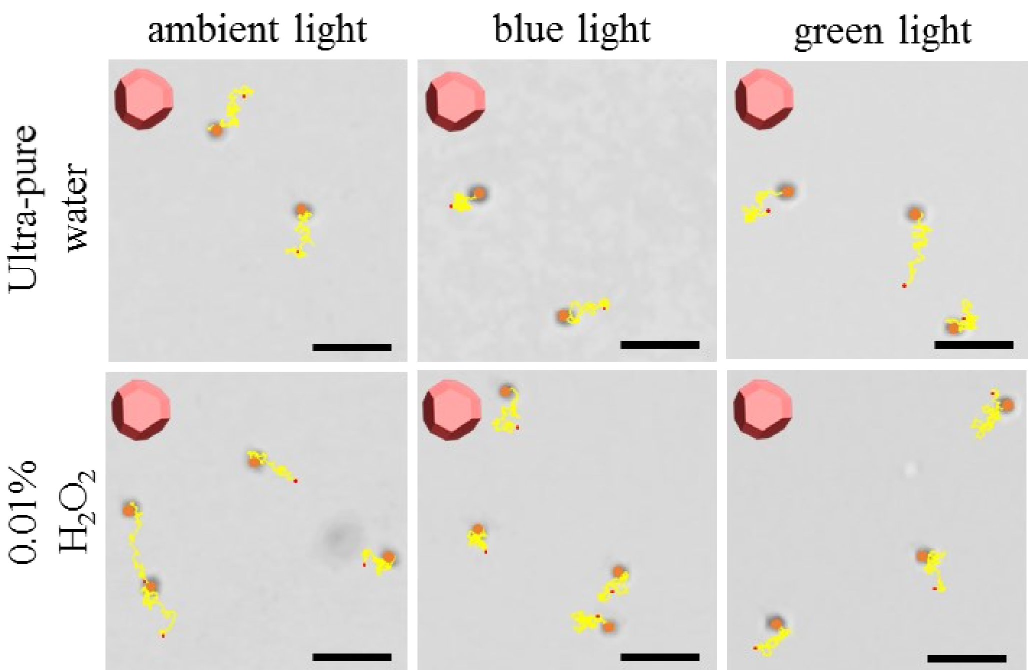

Fig. S10 The imposed video images to illustrate the trajectories of truncated octahedral Cu_2O nanomotors in pure water an in 0.01 v% H_2O_2 solution over 3 seconds. Scale bar: 5 μm.

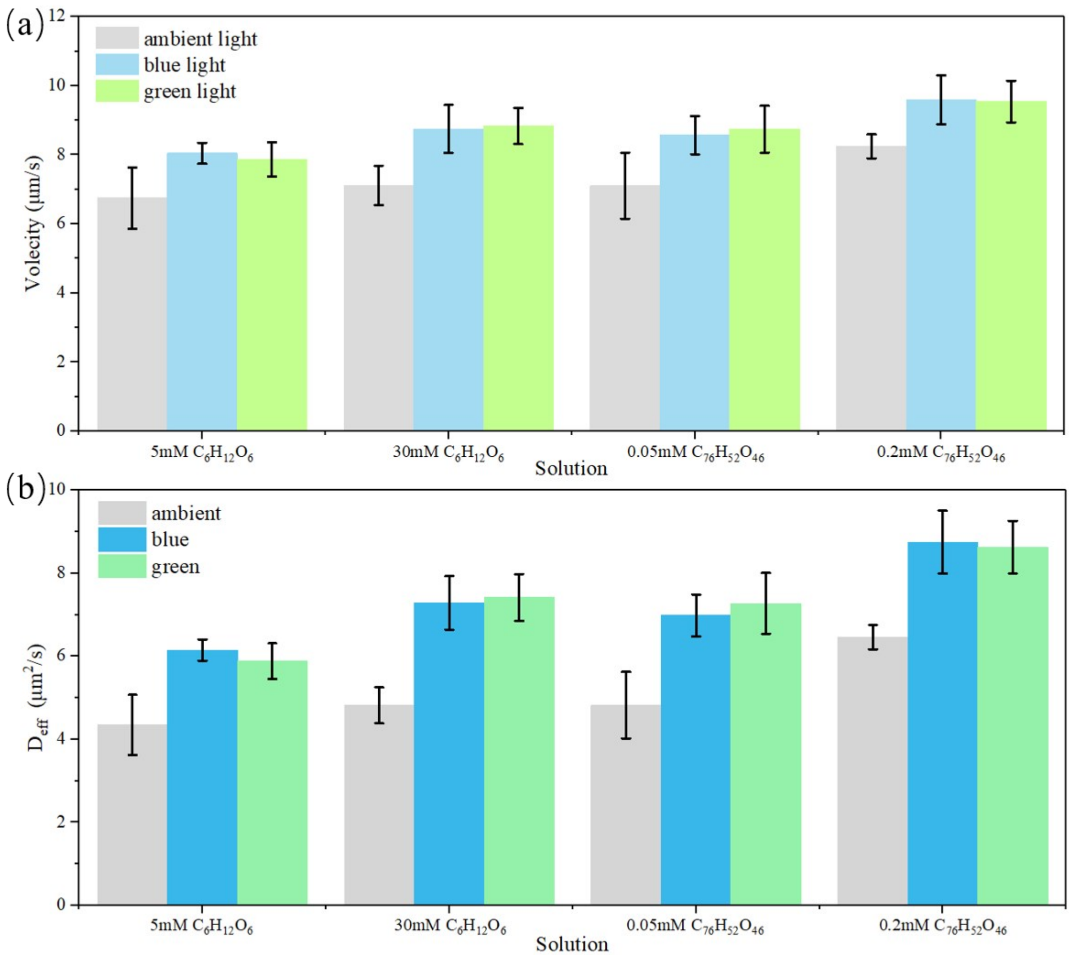

Fig. S11 Velocity (a) and effective diffusion coefficient (b) of truncated octahedral Cu_2O nanomotors in various concentration glucose and tannic acid solutions after exposure of visible light (ambient light, blue light, green light).

Table S1 The lattice constants obtained experimental values. All values are given in Å. a, b, and c are the lattices lengths. α, β and γ are angles.

System	a	b	α	β	γ
Cu_2O(1 1 1)	6.10	6.10	90	90	120
Cu_2O(1 0 0)	4.31	4.31	90	90	90
Cu_2O(2 0 0)	4.31	4.31	90	90	90
Cu_2O(1 1 0)	4.31	6.10	90	90	90

Table S2 Averaged electrostatic potential of the Cu-terminated and O-terminated Cu_2O slabs as a function of z-direct coordinate. The vacuum level was shifted to the zero point. The work function (Φ) $\Phi = E_{vac} - E_f$.

	Cu_2O(1 1 1)	$Cu_2O(1\ 0\ 0)_{Cu}$	$Cu_2O(1\ 0\ 0)_{O}$
E_{vac}	4.45	7.06	6.93
E_F	-0.53	0.42	0.48
Φ	4.98	6.64	6.45

Table S3 The energy band of the Cu-terminated and O-terminated Cu_2O slabs. The Band gap (Φ) $E_g = E_{cbm} - E_{vbm}$

	$Cu_2O(1\ 1\ 1)$	$Cu_2O(1\ 0\ 0)_{Cu}$	$Cu_2O(1\ 0\ 0)_O$
E_{Fermi}	-0.53	0.42	0.48
E_{cbm}	0.40	0.47	-
E_{vbm}	-0.04	0.33	-
$E_{ban\text{-}gap}$	0.44	0.14	-